PAPER

Check for updates

Unveiling the multiscale morphology of chemically stabilized proton exchange membranes for fuel cells by means of Fourier and real space studies†

Natacha Huynh,[ab] João Paulo Cosas Fernandes, [ID][a] Vincent H. Mareau, [ID][a] Laurent Gonon,[a] Stéphanie Pouget, [ID][c] Pierre-Henri Jouneau,[c] Lionel Porcar[d] and Hakima Mendil-Jakani [ID] *[a]

We recently presented the elaboration and functional properties of a new generation of hybrid membranes for PEMFC applications showing promising performances and durability. The strategy was to form, inside a commercial sPEEK membrane, *via in situ* sol–gel (SG) synthesis, a reactive SG phase able to reduce oxidative species generated during FC operation. In order to understand structure-properties interplay, we use a combination of direct space (AFM/3D FIB-SEM) and reciprocal space (SANS/WAXS) techniques to cover dimensional scales ranging from a hundred to few nanometers. AFM modulus images showed the SG phase distributed into spherical domains whose size increases with the SG uptake (*ca.* 100–200 nm range). Using contrast variation SANS, we observed that the sPEEK nanostructure is mostly unaffected by the insertion of the SG phase which presents a fractal-like multiscale structure. Additionally, the size of both the particles (aggregates/primary) is much too large to be sequestered in the ionic pathways of sPEEK. These findings indicate that the SG-NPs mainly grow within the amorphous interbundle domains. Noticeable rightward shift and widening of the ionomer peak are observed with the SG content, suggesting ion channel compression and greater heterogeneity of the ionic domain size. The SG phase develops in the interbundle regions with a limited impact on the water uptake but leading to a discontinuity of ionic conductivity. This Fourier and real spaces study clarifies the structure of the hybrid membranes and brings into the question the ideal distribution/localization of the SG phase to optimize the membrane's stabilization.

Introduction

Proton exchange membranes fuel cells (PEMFCs) are considered as promising power systems for the next generation of electric vehicles operating without emission of any greenhouse gas. Indeed, PEMFC has many attractive features, including high power density, rapid start-up and high efficiency, making it a promising clean energy technology. Although great advances have been made in PEMFC development, improving both the performances and durability of the membrane is critical before any large-scale implementation of this technology.[1–4] Membrane degradation under harsh and/or long-term operating conditions is highly detrimental and ultimately causes the

system failure. In addition, in order to reach faster electrochemical reactions, increase the tolerance of the catalysts to CO poisoning and mitigate the cooling management for PEMFC applications, a higher temperature range (up to 150 °C) is targeted. Yet it is not achievable with benchmark PFSA membranes such as Nafion® due to a loss of the functional properties (thermomechanical properties and proton conductivity if not properly hydrated).

Different strategies have been developed to overcome the main bottlenecks related to polymer membranes for a widespread implementation of PEMFC. However, the design of more durable membranes operating at higher temperatures/low RH is extremely challenging because one key property (conductivity) is generally improved at the expense of the others (lifetime, mechanical properties). For instance, this problem is encountered for the three most promising routes, namely the elaboration of Inter Penetrated Networks (IPN) (one network for the mechanical strength, crosslinked or not, the other for the proton conduction),[5,6] the design of novel block-copolymers[7–10] and the use of fillers/nanocharges and stabilizing additives.[11] Indeed, the proton conductivity is decreased due to phase demixing for the IPN strategy intended to improve thermo-

[a]Univ. Grenoble Alpes, CEA, CNRS, IRIG-SyMMES, 38000 Grenoble, France. E-mail: hakima.mendil-jakani@cea.fr

[b]Université de Lyon, Université Lyon1, UMR CNRS 5223, Ingénierie des Matériaux Polymères, F-69622 Lyon, France

[c]Univ. Grenoble Alpes, CEA, IRIG-MEM, 38000 Grenoble, France

[d]Institut Laue Langevin, F-38042 Grenoble Cedex 9, France

† Electronic supplementary information (ESI) available. See DOI: 10.1039/d1na00005e

mechanical properties. In addition, crosslinked IPN membranes can become brittle while copolymers have a mechanical weakness due to their usually low molecular weight, and their final morphology is hardly predictable. Finally, for hybrid membranes containing fillers/nanocharges and stabilizing additives, issues arise from the introduction, dispersion and possible elution in the exhaust water of these fillers/additives during FC operation, as well as their impact on the proton conductivity, mechanical properties and permeability of the membranes.

The hybridization strategy, however, can provide better control over the nanostructure and functional properties.[12] To name a few, one can cite: (i) an improvement of water retention with hygroscopic particles as ZrP, SiO_2, TiO_2, ZrO_2 (precipitated within pre-formed PFSA and sPEEK membranes or in the polymer dispersion[13,14]), (ii) an enhancement of the mechanical properties with SiO_2 fillers[15–18] for PEMPC, (iii) a reduction of vanadium crossover for vanadium redox flow batteries (again SiO_2 fillers),[19] (iv) or a mitigation of the chemical degradation (cerium-NPs).[20] In addition, the aforementioned issues like the dispersion or elution of fillers/nanocharges can be overcome if a SG network is grown *in situ* in a host ionomer membrane instead of dispersing inorganic particles into an ionomer solution previous to membrane casting.[21]

Indeed, this hybridization process allows for control over the immobilization and localization of the SG phase across the membrane. As shown by Mauritz and coworkers, the hydrophilic/hydrophobic nanophase segregated morphologies of sulfonated membraned can act as an interactive template capable of directing SG hydrolysis/polycondensation of inorganic alkoxides and organoalkoxysilanes.[17,22]

We have recently shown that the SG route is an efficient strategy to physically and chemically stabilize sPEEK membranes which are prone to rapid chemical oxidation and short lifetime in FC (hundreds of hours *vs.* tens of thousands hours for Nafion membrane).[23] A SG phase was grown by self-condensation of (3-mercaptopropyl)trimethoxysilane (MPTMS) inside a commercial sPEEK host membrane in order to (i) improve the mechanical properties of the membrane (limitation of the dimensional changes) and (ii) reduce the oxidative species generated during FC operation, thanks to the mercapto groups carried by each repeat unit which can be oxidized up to the formation of new sulfonated groups.[24–27] This reactive SG phase was therefore designed to evolve positively under the aggressive long-term operating conditions in real devices. If MPTMS has already been used to increase the proton conductivity of PEM by a direct H_2O_2 oxidation of the mercaptan group to sulfonic ones,[24–27] it has never been used so far to neutralize the oxidative species generated in fuel cell. We observed that the hybrid membranes have a better water uptake and proton conductivity than the sPEEK membrane up to a SG uptake of 17%, with a gas permeability slightly higher than the native sPEEK but still lower than the reference Nafion. H_2O_2 accelerated aging tests evidenced the ability of the SG phase to prevent the oxidative degradation of the sPEEK phase. This was confirmed by the fuel cell operability tests showing better and

more durable performances for the hybrid membranes, without any increase of the gas permeability during operation.

In the present paper we focus on the exploration of the structure-properties interplay of these SG hybridized sPEEK membranes, as the morphology (size, interaction/dispersion, connectivity) and localization (polar/apolar regions) of the SG phase inside the host matrix are parameters expected to be crucial for ionic conductivity, gas permeability, chemical stability and mechanical properties of the hybrid membranes. The structural information was obtained by a combination of direct space (co-localized AFM-Raman,[28] AFM and 3D FIB-SEM), and reciprocal space techniques (SANS and WAXS).

Experimental

Hybrid membrane synthesis

To synthesize the hybrid membranes, a SG phase is grown by self-condensation of a MPTMS SG precursor inside a commercial sPEEK host membrane.

Starting material. sPEEK (sulfonated polyetheretherketone) membranes with an IEC of 1.34 meq. g^{-1} were purchased from Fumatech. The SG precursor, (3-mercaptopropyl)trimethoxysilane (MPTMS) was purchased from Aldrich (CAS no 4420-74-0).

Membrane fabrication process. The fabrication steps were detailed in a previous publication and are briefly presented hereafter.[28]

(1) From a pristine to a host sPEEK membrane. Prior to the impregnation, the host sPEEK membranes were re-acidified in a 1 M HCL solution at room temperature for 4 h, triple rinsed with pure water, hydrothermally treated in liquid water at 80 °C for 72 h to improve nano-phase separation between hydrophilic and hydrophobic domains.[29,30] This hydrothermal treatment allows improving the membrane's proton conductivity to make it comparable with the benchmark Nafion®. At this stage, the membrane is labelled sPEEK_NS (NS for NanoStructured). The membranes were then swollen for 24 hours in an acidified (acetic acid addition down to pH = 4) water/ethanol mixture (64/36 volume composition) to condition the membranes prior to SG impregnation.

(2) Sol–gel impregnation/condensation into a host sPEEK membrane (I). Solutions of MPTMS SG precursors in the same solvent mixture as the one used for membrane swelling were prepared separately (stirred for 2 hours) to obtain a homogeneous solution. Hydrolysis of the MPTMS SG precursors took place during this step. The host sPEEK membrane was immersed into this solution during 4 days (at room temperature). Then the membrane was removed from the solution and dried in an oven under a nitrogen flux at room temperature overnight.

(3) Post-condensation of the SG phase to improve its extent of condensation (PC). The hybrid membrane was thermally post-condensed for 24 hours at 70 °C and a relative humidity (R.H.) of 6.3%.

(4) Hydrothermal post treatment to improve the proton conductivity of the hybrid membrane (PT). A hydrothermal post treatment (in liquid water at 80 °C for 72 h) was applied to the

hybrid membrane in order to improve its proton conductivity, and to elute uncondensed SG precursors or entrapped oligomers.

The hybrid membranes are labeled: HyM-X%-PT with X% the SG$_{uptake}$ (see definition below) of the hybrid membrane and PT standing for the last step of elaboration (PT = hydrothermal post treatment).

Co-localized AFM-Raman has shown a lower SG uptake over a thickness of about one micron on both sides of the membrane together with an homogeneous SG phase distribution in the rest of the membrane.[28]

In order to understand the impact of the SG phase on the host membrane's nanostructure, the sPEEK_NS membranes were conditioned along the aforementioned process (from step (2) (without SG precursors introduction in the solvent mixture) to step (4)) to obtain a blank to be compared with the hybrid membranes. The blank membranes are labeled sPEEK_NS_PT (steps I, PC, then PT).

Gravimetric measurements

SG uptake. The SG$_{Upt}$ (eqn (1)) of the hybrid membrane was calculated from gravimetric measurements of the mass of sPEEK_NS (msPEEK_NS$_{dry}$) and mass of the hybrid membrane (mHyM$_{dry}$), in the dry state (dried in an oven under a nitrogen flux at room temperature overnight).

$$SG_{Upt} = \frac{mSG_{dry}}{msPEEK\_NS_{dry}} \times 100\%$$
$$= \frac{mHyM_{dry} - msPEEK\_NS_{dry}}{msPEEK\_NS_{dry}} \times 100\% \quad (1)$$

Water uptake. The hybrid membrane water uptake (W_{Upt}) in liquid water at 25 °C was calculated as follows:

$$W_{Upt} = \frac{mHyM_{wet} - mHyM_{dry}}{mHyM_{dry}} \times 100\% \quad (2)$$

To measure the mass of the water swollen hybrid membrane, mHyM$_{wet}$, excess water on surfaces was removed from the membrane using absorbent paper just before weighing.

Density measurements

The density of each phase was measured with a Accupyc II 1340 gas pycnometer from Micromeritrics. All samples were dried before measurement.

Proton conductivity

The in-plane resistance was measured by voltamperometry, by performing a linear voltage sweep using an Essential VSP Potentiostat (BioLogic Science Instrument) and a BT-110 conductivity clamp (four-electrode method,[31] Scribner Inc., USA) at room temperature and at the swollen state, after equilibrium (at least 24 hours in liquid water). The slope of voltage *vs.* current response was used as the resistance (R in Ω) in the in-plane conductivity, σ (S cm^{-1}), calculated according to eqn (3):

$$\sigma = \frac{L}{W \times e \times R} \quad (3)$$

where L is the distance between the inner V-sense electrodes (cm), W is the membrane width (cm) and e is the membrane thickness (cm).

It should be stressed that the conductivity measurements in the present publication are substantially lower from the ones reported in our previous publication focused on the synthesis of the MPTMS hybrid membranes.[28] Meanwhile we upgraded our home-made conductivity-cell (using impedance spectroscopy) to the four-electrode system described above, giving better accuracy and reproducibility. This has no impact on the discussion of the results previously published, however no comparison should be made between these two sets of data.

Multiscale morphology

Atomic force microscopy (AFM). Topographic and mechanical images of the hybrid membranes were obtained using PeakForce QNM mode on a Nanoscope Dimension ICON AFM (Bruker). All measurements were made under ambient conditions (room temperature and relative humidity of about 50%) with a standard cantilever holder for operation in air. In order to image the sample, the tip (see tip references below) was oscillated in the z-direction (travel distance of 150 nm) at 2 kHz (2000 force–distance curves per second) while scanning the sample line by line at scan rate of 0.977 Hz. Images were taken with a resolution of 512 × 512 pixels (average of 2 force–distance curves per pixel). Thus each image corresponds to about half a million force–distance curves, distributed over the scanned surface (10 × 10 μm^2 or 1 × 1 μm^2). AFM images were analyzed using Nanoscope Analysis version 1.7. A relative calibration method was performed using a dedicated reference samples kit provided by Bruker (Model: PFQNM-SMPKIT-12m). The deflection sensitivity was first measured doing a ramp on a standard sapphire sample and the spring constant of the cantilever was determined using the Thermal Tune method. Using the polystyrene-low density polyethylene (PS-LDPE) standard sample, the deflection sensitivity was evaluated in order to confirm the proper difference between the polyethylene (LDPE) and the polystyrene (PS) modulus ($\Delta \log E \sim 1.4$) and the tip radius was adjusted to obtain the proper value of 2.7 GPa for the PS. Cantilevers' spring constant used in this study varied from 30–40 N m^{-1} for RTESPA Bruker model and 0.2–0.8 N m^{-1} for ScanAsyst Air probes. A peakforce setpoint value of 50–100 nN was used, inducing deformation depths of 2–10 nm for all samples, in order to have a good correlation between the modulus values of the references, but also to operate within the limits of the DMT model used by Nanoscope Software to calculate the mechanical properties from the force–distance curves. The cryo-ultramicrotomy procedure provided access to unmodified cross-section (no compressive forces, no shearing) with a very low roughness (very flat samples).

3D-FIB-SEM. 3D-FIB-SEM investigations were performed on a Zeiss crossbeam 550 FIB-SEM microscope, a scanning electron microscope combined with a focused gallium ion beam column for serial FIB milling and imaging. The previously cryo-

ultramicrotomed surfaced HyM-32%-PT membrane was imaged in SEM using Secondary Electrons (SE), with an In-Lens detector for the topographic image, and Backscattered Electron (BSE) for complementary chemical contrast. The images were taken with an optimized acceleration voltage of 1.5 kV and detector working distance of 4.9 mm. Serial sectioning involved the removal of a volume of the material by the ion beam followed by an image with the electron beam. First the membrane's surface was milled until the core was attained. Then, 500 images were taken over a depth of 2.5 μm, which means that 5 nm of the membrane was milled away before each SEM image.

Small Angle Neutron Scattering (SANS). SANS measurements were carried out on the D22 spectrometer at the Institut Laue Langevin, Grenoble, France. The incoming wavelength was $\lambda = 6$ Å. Sample-detector distances of 2.8 m and 17.6 m were used to cover the extended range of momentum transfer $2.5 \ 10^{-3} < Q < 0.4$ Å^{-1}, allowing to probe sizes and correlations in the range of 16 to 2500 Å. Q is the scattering vector defined as $Q = (4\pi/\lambda) \sin(\theta/2)$ where λ is the wavelength of the incident neutron beam and θ is the total scattering angle. The 2D patterns were isotropic and thus radially averaged to extract the 1D scattered intensities $I(Q)$. The SANS $I(Q)$ spectra were corrected for detector efficiency, background and empty cell subtraction. Absolute intensities were obtained by measuring the direct beam through a calibrated attenuator. Prior to SANS experiments, the hybrid membranes were equilibrated in H_2O, D_2O or a mixture of both for at least 24 h. Thicknesses of the hydrated samples (stack of 3 membranes) were measured using a micrometer and were taken as the average of at least four measurements on the sample. The hydrated samples were then mounted in a 1 mm-gap cell with quartz windows. The sealing was ensured with O-rings.

Wide angle X-ray Scattering (WAXS)

The Wide-Angle X-ray Scattering (WAXS) patterns were recorded using a Panalytical X'Pert diffractometer at CEA-Grenoble/IRIG,

equipped with a copper X-ray tube ($\lambda K_{\alpha 1} = 1.5418$ Å) delivering a linear beam and with a 1D X'Celerator detector. A 0.5° divergence slit was used on the primary path with a set of anti-scattering slits before and after the sample. The axial divergence was limited by 0.02 rad Soller slits. The measurements were performed in $\theta/2\theta$ transmission geometry. The data were recorded for 2θ ranging from 5° to 60° (0.35 to 4 Å^{-1}). The samples were equilibrated at room temperature and relative humidity.

Results and discussion

It is well established that the membranes' functional properties (ionic conductivity, permeability to gases and mechanical properties) strongly depend on their microstructure. In order to decipher the structure-properties interplay, we scrutinized the microstructure of the membranes by a combination of direct space and reciprocal space techniques to cover dimensional scales that range from a hundred to a few tenths of a nanometer. To do so, we utilized co-localized AFM-Raman,[28] AFM, SANS, and WAXS. Complementarity between these techniques allows cross validation thereby increasing the reliability of the described morphology. We characterized hybrid membranes with different SG uptakes (10%, 20% and 32%, hereafter labeled HyM-10%-PT, HyM-20%-PT and HyM-32%-PT).

Real space morphological characterization of the hybrid membranes by AFM and 3D-FIB-SEM

AFM experiments were performed on cryo-ultramicrotomed cross-sections (not the ultrathin section but the opened membrane following the procedure presented in a previous work[32]). Fig. 1 shows AFM modulus images (10×10 μm^2 and 1×1 μm^2) of hybrid membranes with a SG uptake of: 0% ((a) and (d)), 20% ((b) and (e)) and 32% ((c) and (f)). Scale bars are given to distinguish 10×10 μm^2 from 1×1 μm^2.

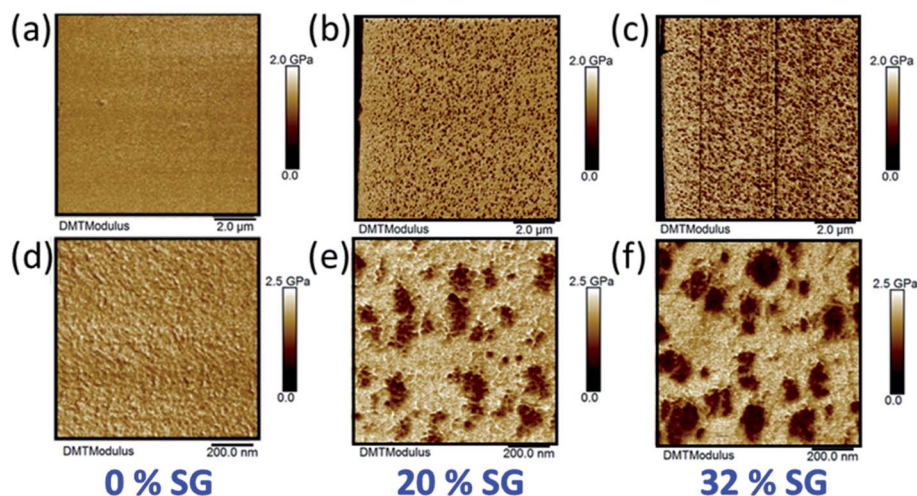**Fig. 1** AFM modulus images of sPEEK_NS (a), (d); HyM-20%-PT (b), (e) and HyM-32%-PT (c), (f). 10×10 μm^2 images are presented from (a) to (c) and 1×1 μm^2 images from (d) to (f).

Table 1 Modulus of each phase of the hybrid membranes (AFM)

Sample	D_{AFM} (Å)	sPEEK modulus (GPa)	SG modulus (GPa)
HyM-20%-PT	1100 ± 480	1.9 ± 0.1	0.89 ± 0.05
HyM-32%-PT	1350 ± 630	1.9 ± 0.1	0.85 ± 0.05

From the 10×10 μm^2, it is clearly observed that the SG phase is organized into spherical-shaped domains. The mean diameter of SG domains (D_{AFM}) measured on the 10×10 μm^2 images was found to be: 1100 ± 480 Å and 1350 ± 630 Å, for HyM-20% and HyM-32%, respectively. As expected from a nucleation and growth process, D_{AFM} increases with the SG uptake. D_{AFM} as well as the sPEEK and SG modulus measured on the 1×1 μm^2 images (Fig. 1(d)–(f)) are presented on Table 1. The SG phase was found with a modulus of about 0.9 ± 0.1 GPa and the sPEEK phase with a modulus of about 1.9 ± 0.1 GPa.

The modulus of the host sPEEK membrane and the one of the *ex situ* SG phase (homopolymerized MPTMS) taken separately were measured by AFM at 1.9 ± 0.1 GPa and 0.9 ± 0.1 GPa respectively. The moduli of the sPEEK and SG phases within the hybrid membranes do not vary significantly with the SG content and are similar to those of the phases alone. It can therefore be concluded that each phase remains relatively pure upon hybridization. In other words, even if the presence of a limited amount of sPEEK inside the SG domains should not be excluded, this indicates that the two phases coexist without significant mixing at this scale. On the 1×1 μm^2 images (Fig. 1(e) and (f)) one can see that the SG domains do not appear massive, but more like aggregates of smaller particles. To verify this latter assumption and the fact that the SG phase does not form an interconnected network, 3D-FIB-SEM experiments were performed on the sample HyM-32%-PT. Fig. 2(a) shows the milled area of the membrane to access its core for 3D analysis. Fig. 2(b) presents one of the BSE images of the stack (3×3 μm^2), and Fig. 2(c) is an enlargement of a selected area of this figure (1×1 μm^2). These BSE images confirm the AFM observation of SG aggregates being formed by smaller particles, with a chemical contrast for BSE images complementary to the mechanical contrast of AFM images. The SG phase contains

silicon atoms, absent in the sPEEK phase. The brighter the area on the BSE image, the more it contains silicon (higher atomic number: 14 for silicon *versus* 8 for oxygen and 6 for carbon), and therefore SG. The stacks of SE and BSE images corresponding to a volume of $3 \times 3 \times 2.5$ μm^3 are shown in ESI.† They reveal that the SG domains are not interconnected but rather individually dispersed in the sPEEK matrix, thus confirming the AFM observations.

The formation of SG-rich phase is in accordance with the ability of acid-catalyzed SG derived silica materials to form fractal structure created by large particles (secondary particles/aggregates) which are also clusters of smaller primary particles.[33]

In addition to the AFM and 3D-FIB-SEM experiments, we performed scattering techniques (SANS/WAXS) in order to provide a multiscale description of the impact of the SG phase on the host membrane nanosegregated morphology (ionic/crystalline/amorphous phases) and on the hierarchical structure of the SG phase (typical size of the primary particles and their distribution). WAXS measurements performed on sPEEK_NS_PT, an *ex situ* synthesized SG sample and HyM-32%-PT (see ESI-2†) show that the hybrid membrane pattern can be mainly considered as the sum of the patterns of the polymer and sol–gel components, confirming the absence of structural modifications in the hybrid membrane at a scale ranging from a few Å up to a few nm.

Fourier space morphological characterization of the hybrid membranes

In the case of condensed and dispersed particles consisting of homogeneous isotropic scattering centers, the scattered intensity $I(Q)$ contains information on the particles shape (form factor $P(Q)$) and organization (structure factor $S(Q)$). For N_p centrosymmetric particles of volume V_p the intensity per unit volume V writes:[34,35]

$$I(Q) = \frac{V_p^2}{V} N_p \Delta\rho^2 P(Q) S(Q) = \Phi V_p \Delta\rho^2 P(Q) S(Q) \quad (4)$$

with Φ the particle volume fraction and $\Delta\rho^2$ the so-called contrast factor, determined by the difference in the scattering
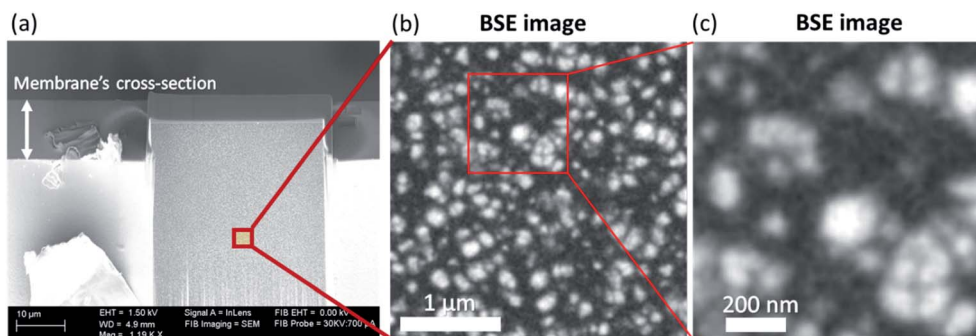

Fig. 2 (a) SEM image of the milled area of the membrane HyM-32%-PT; (b) BSE image extracted from the stack of images obtained (3×3 μm^2) and (c) BSE image enlargement of a selected area of (b) (1×1 μm^2). The stacks of SE and BSE images obtained from this 3D-FIB-SEM experiment are available as ESI-1.†

length density (SLD) between the particles and the medium ρ_1 and ρ_2 respectively with $\rho = dN_Ab/M$, where d is the mass density, N_A the Avogadro constant and b the neutron scattering length and M the molecular weight of the repeat unit.

A series of contrast variation Small Angle Neutron Scattering (SANS) experiments was performed on hydrated hybrid membranes. This experiment consists in recording the SANS profiles of membranes equilibrated with different H$_2$O–D$_2$O solvent mixtures to vary the contrast between the polymer phase, the SG phase and the solvent. It is possible to continuously adjust the scattering length density (SLD) of the solvent in order to match out selectively the SLD of a component (either the polymer or the SG phase), making it invisible to neutrons. This contrast variation strategy, which can be applied thanks to the hydrophilicity of the ionic domains, constitutes a considerable advantage in terms of cost and feasibility over the selective deuteration of polymers because many useful deuterated monomers are not commercially available or prohibitively expensive.

The neutron SLD (ρ) of the different phase were calculated (using the molecular weight of the repeat units and densities of both sPEEK and SG powder obtained by polycondensation of MPTMS, respectively $M_{\text{sPEEK}} = 320$ g mol^{-1}, $d_{\text{sPEEK}} = 1.4$ g cm^{-3} and $M_{\text{SG}} = 127.2$ g mol^{-1}; $d_{\text{SG}} = 1.26$ g cm^{-3}) and were found equal to $\rho_{\text{sPEEK}} = 2.75 \times 10^{10}$ cm^{-2} and $\rho_{\text{SG}} = 0.62 \times 10^{10}$ cm^{-2}. The solvent mixture corresponding to the SLD of the sPEEK and SG phase are respectively 50% H$_2$O–50% D$_2$O and 83.5% H$_2$O–16.5% D$_2$O by volume (hereafter abbreviated as 50% D$_2$O and 16.5% D$_2$O for the sake of brevity). The calculated SLDs were cross-checked experimentally by performing contrast variation SANS on each component. Each phase was equilibrated in different H$_2$O–D$_2$O solvent mixtures; the square root of the total intensity was plotted as a function of the solvent SLD or equivalently, the D$_2$O content (eqn (3)). The SLD of the phase corresponds to the composition for which the signal vanishes, *i.e.*, the contrast match point. Table 2 gathers the calculated SLDs and contrast terms.

Impact of the SG phase on the host membrane nanostructure

Contrast variation experiments were performed to match out the SG signal (hybrid membranes equilibrated in a 16.5% D$_2$O mixture). Fig. 3 compares the SANS profiles of HyM-10%-PT, HyM-20%-PT and HyM-32%-PT equilibrated in 16.5%D$_2$O and
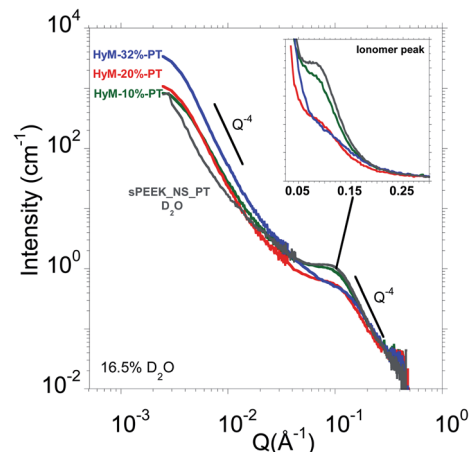

Fig. 3 SANS profiles at room temperature of HyM-10%-PT (□), HyM-20%-PT (□), HyM-32%-PT (□) in 16.5% D$_2$O. The SANS profile of sPEEK_NS_PT (D$_2$O) (□) is added for comparison. The insets are zoom of the ionomer peak.

the one of sPEEK_NS_PT in D$_2$O (the SANS profile of a nano-structured sPEEK in H$_2$O is very similar to the one recorded in D$_2$O).[36] This membrane conditioning ensures to reach swelling equilibrium.[30]

As expected, the SANS profile of the sPEEK_NS_PT displays a well-defined ionomer peak (located at $Q_{\text{iono}} \sim 0.1$ Å^{-1} associated to an inter-domain spacing $d_{\text{iono}} = 2\pi/Q_{\text{iono}} \sim 63$ Å), which is the fingerprint of the nanophase separation between hydrophilic and hydrophobic domains.[29] At larger angles, a Q^{-4} Porod's law is observed, which is the signature of well-defined interfaces between hydrophilic and hydrophobic phases.[29,30] At this stage, it is therefore worth reminding the similarities in terms of microstructure between sPEEK and Nafion®. The Nafion® microstructure is still the subject of debates[37,38] but the ribbon-like polymer particle model of Rubatat *et al.* appears as the most suitable model to describe the main structural features of Nafion® together with its transport properties.[39–43] The local structure is formed by polymer ribbons with the ionic groups at the water–polymer interface. These ribbons are locally oriented and are packed into randomly distributed bundles of 50–100 nm (estimated from USAXS and AFM[40]) which give rise to a typical small angle upturn (related to the large-scale heterogeneities in the electron density associated with the disordered distribution of ionic domains).[39,40,44] The same was concluded for sPEEK after achieving good nanophase separation.[29,30] Indeed, the scattering entities of sPEEK were found to be compatible with flat aggregates (ribbon-like), as expected for most of the dissociated ionomers.[45]

The SANS profiles of the hybrid membranes soaked in a 16.5% D$_2$O mixture display similar scattering behavior: a small angle upturn followed by an ionomer peak which shows that the original phase separated morphology of the host sPEEK matrix persists despite the insertion of the SG phase, which is essential to ensure proton conduction.

Similar results were obtained on SAXS and SANS analyses of Nafion®/SG-derived silicon oxide phase, obtained either by membrane casting or by *in situ* SG reaction.[13,15,18,19]

Table 2 Calculated scattering length density ρ (SLD) of the different phases and contrast factors ($\Delta\rho^2$). SLDs are calculated from the molecular weight of the repeat units and density of sPEEK and the solid obtained by polycondensation of MPTMS, respectively $M_{\text{sPEEK}} = 320$ g mol^{-1}, $d_{\text{sPEEK}} = 1.4$ g cm^{-3} and $M_{\text{SG}} = 127.2$ g mol^{-1}; $d_{\text{SG}} = 1.26$ g cm^{-3}

Phase	ρ (10^{10} cm^{-2})	$\Delta\rho^2$ (10^{10} cm^{-2})	
		sPEEK	SG
sPEEK	2.75	—	4.55
SG	0.62	4.55	—
50% D$_2$O	2.92	≈0	5.30
16.5% D$_2$O	0.59	4.65	≈0

Table 3 Ionomer peak position Q_{iono} (± 0.01) and corresponding correlation length $d_{iono} = 2\pi/Q_{iono}$ for the different membranes swollen in pure water at room temperature then conditioned in a 16.5% D_2O mixture for the hybrid membranes and in D_2O for sPEEK_NS_PT for SANS measurements (room temperature)

Sample	Q_{iono} (Å^{-1}) (± 0.01)	d_{iono} (Å)
sPEEK_NS_PT	0.10	63 ± 6
HyM-10%-PT	0.10	63 ± 6
HyM-20%-PT	0.11	57 ± 5
HyM-32%-PT	0.12	54 ± 4

Concerning the intensity, shape and position of the ionomer peak, we observe a clear dependence with the SG content. A zoom of the ionomer peaks is presented in the inset of Fig. 3. A significant ionomer peak broadening and shifting to higher Q is observed when increasing SG loading for SG uptakes greater than 10%. In other words, the SG content's increase results into a tightening of the ionic domains together with an increase of their size heterogeneity. The ionomer peak's positions Q_{iono} and the corresponding correlation length d_{iono} are displayed in Table 3.

From these measurements, indications about the SG aggregates' localization can be deducted. Indeed, the tightening of the ionic domains can be explained by a compression of the polymeric aggregates exerted by the expansion of the SG aggregates. The latters therefore likely reside within the interbundle areas where the spatial arrangement of the polymer ribbons is less compact[39,40] making it compatible to accommodate large aggregates (observed by AFM) as also suggested in the work on Zr–P particles formed by *in situ* precipitation in Nafion®.[13]

Hierarchical mesostructure of the SG phase, the case of HyM-32%-PT

In order to measure solely the SG signal, HyM-32%-PT was soaked in 50%D_2O which corresponds to the contrast match point of the sPEEK phase.[36] Fig. 4 displays the corresponding SANS profile.
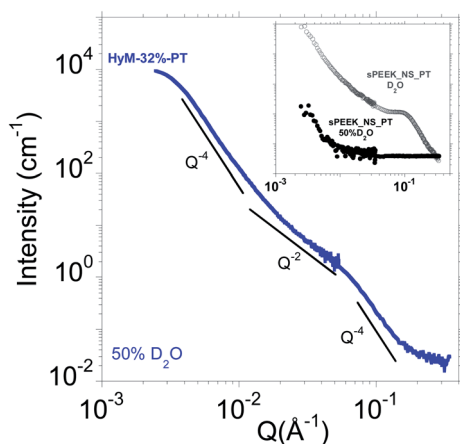
The inset of Fig. 4 compares the SANS profiles of a sPEEK_NS_PT equilibrated in pure D_2O and in 50% D_2O. No signal was measured except the small angle upturn associated to long-range heterogeneities that cannot be completely matched out; the associated intensity is negligible, *i.e.*, between two and three orders of magnitude lower than the scattered intensity for hybrid membranes (depending on the SG uptake, see Fig. 5). This confirms that this solvent composition corresponds to the match point where the contrast is zero, *i.e.*, sPEEK membrane is essentially invisible to neutrons. Therefore, the features observed in the SANS profile of hybrid membranes equilibrated in a 50% D_2O originate solely from the SG phase if both sPEEK and SG phase do not mix resulting in a third phase with an intermediate SLD. The fact that the two components sPEEK and SG are successfully matched independently is a further indication of the absence of mixture of the sPEEK and SG phases at this scale. This result supports the hypothesis that the SG phase mainly developed in the interbundle areas (free volume available for large aggregates, observed by AFM and 3D-FIB-SEM).

As expected from AFM and 3D-FIB-SEM analyses showing that the SG phase is aggregated into homogeneously dispersed spherical-shape aggregates on the order of 1000 Å, the low-Q signal obeys scattering of high-polydispersity spherical objects, with almost constant intensity of the low-Q region (*i.e.* $I(Q)$ scales with Q^{-0}), followed by a Q^{-4} Porod behavior without oscillations. The absence of correlation peak at small angles confirms that the large spherical objects are dispersed without any significant correlation in position or orientation.

The high intensity and the low angular position of this signal is coherent with the SG aggregates size observed by AFM and 3D-FIB-SEM, of the order of a hundred nanometers. Considering the size of these aggregates, ranging from ~1000 to 1400 Å, it is clear that they are much too large to be sequestered within ion conducting channels typically 20 times smaller[29] which confirm the previous conclusions. Once again, the formation of some small SG-NPs within the ionic domains
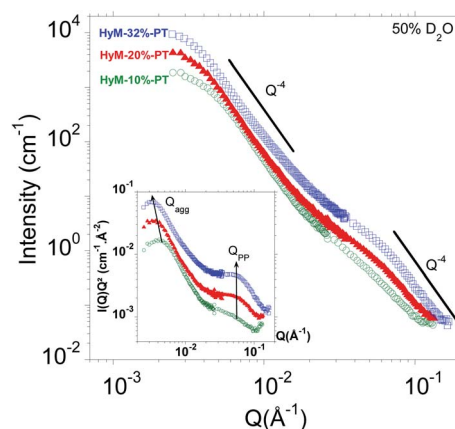

Fig. 4 SANS profile (room temperature) of HyM-32%-PT in 50% D_2O. The Q^{-4} and Q^{-2} slopes are eye-guides. The inset compares the SANS profiles (room temperature) of a sPEEK_NS_PT in D_2O (x̂) and in 50% D_2O (●).

Fig. 5 SANS profiles at room temperature of HyM-10%-PT (○), HyM-20%-PT% (▲) and HyM-32%-PT (□) in 50% D_2O. The Q^{-4} and Q^{-2} slopes are eye-guides. The inset displays the Kratky plot $I(Q)Q^2$ *vs.* Q. The arrows illustrate the evolution of the peak positions Q_{agg} (aggregates) and Q_{PP} (primary particles) with the SG content.

cannot be excluded, considering the hydrophilicity of the hydrolyzed SG precursors.

At larger angles, a bump is observed at about $Q \sim 5.8 \times 10^{-2}$ Å^{-1}, a position independent of the SG uptake (see Fig. 5). This signal is associated to the presence of primary particles (PP); the SG phase is multiscale organized. This is in agreement with the ability of acid-catalyzed SG based materials to form fractal structure created by aggregates which are clusters of primary particles. In addition, the fact that the Young modulus of the SG aggregates (AFM) is similar to the one of the *ex situ* SG phase strongly suggests that the primary particles are densely packed. Therefore, this bump is attributed to the interaction peak between the primary spherical SG particles.

Hierarchical mesostructure of the SG phase, impact on the SG content

What is the typical size of the aggregates and primary particles aggregates? In order to address this question, we recorded the SANS profiles of HyM-10%-PT, HyM-20%-PT and HyM-32%-PT hydrated in 50% D$_2$O. Fig. 5 shows the corresponding SANS profiles.

As expected, differences of intensities and position of the breaks in slope are clearly noticed in the SANS profiles when the SG uptake varies. Very similar scattering profiles are observed. This indicates that the SG content does not significantly influence the SG phase morphology but mainly drives the characteristic sizes of the SG aggregates.

Usually, a Guinier plot ($\ln[I(Q)]$ *vs.* Q^2) allows estimating the radius of gyration R_g of nanoparticles (where the slope of the linear fit of the low-Q region equals $R_g^2/3$).[34] However, for the aggregates, we have no data point for $Q < 2.10^{-3}$ Å^{-1} where this holds true ($R_g Q < 1$, estimation of R_g from AFM by $R_g = \sqrt{\frac{3}{5}} R$, R being the geometric radius of spherical particles). Instead, we therefore used the Kratky representation, which consists in plotting $I(Q)Q^2$ against Q, and allows observing breaks in slope as well-defined maxima. The inset of Fig. 5 displays the corresponding Kratky plots highlighting two peaks associated to the aggregates (at small angles) and to the primary particles (at wider angles). The radius of gyration R_g of the aggregates are calculated from the peak maximum $R_g = \sqrt{3}/Q_{max}$.[34] The mean separation distance between primary particles d_{PP}, which is very likely their diameter D_{PP_SANS}, is deduced from the peak position Q_{PP} from $d_{PP} = D_{PP\text{-}SANS} = 2\pi/Q_{PP}$. The data are gathered in Table 4.

The mean diameter of the SG aggregates measured by SANS and AFM modulus images are in very good agreement. For the lowest SG uptake, the number of primary particles within an aggregate ($(D_{agg}/D_{PP})^3$) is mainly proportional to the SG uptake while it increases less rapidly for higher SG content. This observation suggests that the size of the SG aggregates may be limited by the accommodation of the sPEEK matrix (mechanical resistance and deformation of the polymeric aggregates, free volume). The size of the primary particles remains independent ($D_{PP\_SANS} \sim 11$ nm) of the SG uptake, which is an expected result. The primary particles are also too large to reside within the ionic domains.

In a nutshell, AFM, 3D FIB-SEM, SANS and WAXS experiments show that the sPEEK and SG phase coexist as two independent phases without significant interaction.

Macroscopic properties

In this section we will study the potential correlation between the microstructure and the macroscopic properties of interest.

Fig. 6(a) and (b) display the evolution of the water uptake and the proton conductivity against the hydrophilic volume fraction (sPEEK phase) in order to highlight the contribution of the conducting phase. It has to be noticed that after the hydrothermal treatment, all the membranes were kept at least 24 h in liquid water at room temperature before measurements. As previously published,[30] these storage conditions ensure the stability of structure, swelling and conductivity of sPEEK membranes (swollen sPEEK membranes are in their glassy state at room temperature).

It is observed on Fig. 6(a) that the water uptake increases almost linearly with the volume fraction of the conductive phase Φv_{sPEEK}. This result is consistent with our previous publication showing a similar phenomenon for water vapor sorption experiments.[28] This suggests that the polysiloxane phase does not hinder the accessibility of water to the ionic SO$_3$H groups and exhibits itself a very limited water sorption. It should be noticed however, that the conductivity shows a break in its linear evolution with Φv_{sPEEK}: a sharp (but however limited) decrease of conductivity is observed even for very limited SG uptake, while the rest of the evolution is however linear (Fig. 6(b)).

The decrease in conductivity with the increase of the SG phase content can be explained by the combined effect of the decrease in the sPEEK content, useful for proton transport and the compression of the ionic domains (SANS result, Table 3). However, the observed conductivity drop even with limited SG uptake, indicates that the development of the SG phase in the interbundle regions is certainly responsible for an interruption of the conduction paths in these zones which moderately participate to the proton conduction.[46]

Table 4 Peak position of the maximum in the Kratky plots and diameter of the spherical secondary (aggregate) and primary particles (respectively Q_{agg_SANS} and $D_{agg\text{-}SANS}$, Q_{PP_SANS} and D_{PP_SANS}) of the SG phase within HyM-10%-PT, HyM-20%-PT and HyM-32%-PT determined by SANS analysis

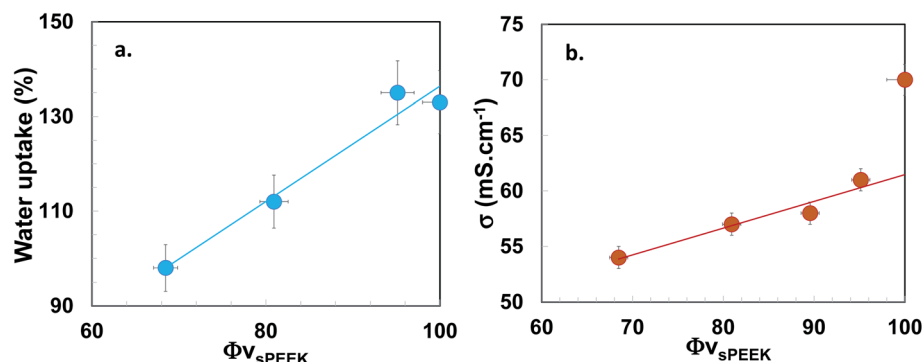| Sample	Q_{agg_SANS} (±0.1) (10^{-3} Å^{-1})	D_{agg_SANS} (Å)	Q_{PP_SANS} (±0.1) (10^{-2} Å^{-1})	D_{PP_SANS} (Å)
HyM-10%-PT	4.4	1016 ± 23	5.8	108 ± 2
HyM-20%-PT	3.5	1280 ± 37	5.8	108 ± 2
HyM-32%-PT	3.2	1400 ± 44	5.8	108 ± 2

Fig. 6 Evolution of the (a) water uptake (●) and (b) proton conductivity (●) of the membranes as a function of the volume fraction of the conductive phase Φv_{sPEEK} measured at room temperature after a swelling in liquid water at 80 °C for 72 h. The straight lines are eye guides.

Conclusions

The aim of the present work was to provide correlations between microstructure and functional properties for a new generation of PEMFC hybrid membranes holding promise for improved durability and performances. The strategy was to grow a SG phase by self-condensation of (3-mercaptopropyl) trimethoxysilane (MPTMS) inside a commercial sPEEK host membrane in order to protect the membrane by reducing the oxidative species generated during FC operation, thanks to the mercapto groups carried by each repeat unit which can be oxidized up to the formation of additional sulfonated groups.

We provided in-depth insights into their multiscale morphology by a combination of direct space (AFM/3D FIB SEM) and reciprocal space (SANS/WAXS) techniques (~100 to a few nm) performed on hybrid membranes with ~10, 20 and 32% SG content.

AFM and 3D-FIB-SEM analyzes showed that the SG phase is organized into spherically shaped aggregates whose size increases with the SG uptake (diameters about 100–200 nm). These aggregates are much too large to reside within ionic pathways of sPEEK membrane (diameters about 3–6 nm).

We used contrast variation SANS to provide a multiscale description of the impact of the SG phase on (i) the host membrane nanosegregated morphology (ionic/crystalline/ amorphous phases) and (ii) the hierarchical structure of the SG phase (typical size of the constitutive particles/distribution).

Matching the SG phase signal (16.5% D_2O, $\rho_{SG\_calc} \approx 0.62 \times 10^{10}$ cm^{-2}), we observed that despite SG insertion, the ionomer peak, the fingerprint of the hydrophilic/hydrophobic nano-phase segregation is still observed, proving that the sPEEK ionic pathways are conserved. Noticeable rightward shift and widening of the ionomer peak are observed with the SG content, which suggest ion channel compression and greater heterogeneity of the ionic domains size.

With sPEEK matching conditions (50% D_2O: $\rho_{50-50} = 2.92 \times 10^{10}$ cm$^{-2} \approx \rho_{sPEEK} = 2.75 \times 10^{10}$ cm^{-2}; no ionomer peak), we observed that the SG phase is multiscale organized, showing its fractal-like nature (aggregates which are clusters of smaller primary particles).

We found that the mean diameter of the SG aggregates measured by AFM modulus images and SANS are in very good agreement. The size of the primary particles determined by SANS remains constant (about 11 nm). We concluded that SG aggregates/primary particles are much too large to be compatible with the dimensions of the ionic pathways of sPEEK (~3–6 nm).

The cross-correlation of AFM, 3D-FIB-SEM and SANS analyses strongly indicates that the SG aggregates mainly grow within the interbundle areas (free volume available for large particles growth). AFM, 3D-FIB-SEM, SANS and WAXS results show that the sPEEK and SG phases coexist as two independent phases without significant interaction.

Finally, the microstructural behavior was naturally correlated to the macroscopic properties of interest, i.e. the water uptake and the proton conductivity. While we observed that the water uptake increases almost linearly with the volume fraction of the ionic phase Φv_{sPEEK}, the conductivity increase is linear only if we exclude the pure sPEEK membrane. Indeed a jump of conductivity is observed for $\Phi_{vsPEEK} = 100\%$. This conductivity drop supports the proposed morphological description of the hybrid membranes, with a SG phase that develops in the interbundle region: limited impact on the water access to the ionic sPEEK phase, however a partial interruption of the ionic path previously connected through the interbundle regions.[46]

With this work, we are confident to optimize the design of alternative hybrid membranes by tailoring the chemistry of the SG precursors (reactivity of the stabilization group, number of hydrolysable functions) and the morphology of the host membrane to optimize the architecture/properties/durability interplay for improved PEMFC performances.

Conflicts of interest

There are no conflicts to declare.

Acknowledgements
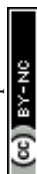
Notes and references

1 R. Borup, J. Meyers, B. Pivovar, Y. S. Kim, R. Mukundan, N. Garland, D. Myers, M. Wilson, F. Garzon, D. Wood, P. Zelenay, K. More, K. Stroh, T. Zawodzinski, J. Boncella, J. E. McGrath, M. Inaba, K. Miyatake, M. Hori, K. Ota, Z. Ogumi, S. Miyata, A. Nishikata, Z. Siroma, Y. Uchimoto, K. Yasuda, K. I. Kimijima and N. Iwashita, *Chem. Rev.*, 2007, **107**, 3904–3951.

2 U. Babic, M. Suermann, F. N. Büchi, L. Gubler and T. J. Schmidt, *J. Electrochem. Soc.*, 2017, F387–F399.

3 A. Albert, T. Lochner, T. J. Schmidt and L. Gubler, *ACS Appl. Mater. Interfaces*, 2016, 15297–15306.

4 L. Dubau, L. Castanheira, F. Maillard, M. Chatenet, O. Lottin, G. Maranzana, J. Dillet, A. Lamibrac, J. C. Perrin, E. Moukheiber, A. Elkaddouri, G. De Moor, C. Bas, L. Flandin and N. Caqué, *Wiley Interdisc. Rev.: Energy Environ.*, 2014, 540–560.

5 V. Delhorbe, X. Thiry, C. Cailleteau, E. Mourier, M. Bathfield, L. Chikh, O. Fichet, B. Ameduri, R. Mercier, S. Vidal, L. Augier, E. Espuche, F. Gouanvé, G. Gebel and A. Morin, *J. Membr. Sci.*, 2012, 57–66.

6 V. Delhorbe, S. R. Reijerkerk, C. Cailleteau, M. Bathfield, L. Chikh, F. Gouanve, L. Ogier, E. Espuche, B. Ameduri, S. Vidal, G. Gebel, A. Morin and O. Fichet, *J. Membr. Sci.*, 2013, 168–180.

7 N. Li and M. D. Guiver, *Macromolecules*, 2014, 2175–2198.

8 Y. A. Elabd and M. A. Hickner, *Macromolecules*, 2011, 1–11.

9 L. Assumma, H. D. Nguyen, C. Iojoiu, S. Lyonnard, R. Mercier and E. Espuche, *ACS Appl. Mater. Interfaces*, 2015, 13808–13820.

10 L. Assumma, C. Iojoiu, R. Mercier, S. Lyonnard, H. D. Nguyen and E. Planes, *J. Polym. Sci., Part A: Polym. Chem.*, 2015, 1941–1956.

11 D. J. Jones and J. Rozière, *Adv. Polym. Sci.*, 2008, 219–264.

12 C. Laberty-Robert, K. Vallé, F. Pereira and C. Sanchez, *Chem. Soc. Rev.*, 2011, 961–1005.

13 D. Truffier-Boutry, A. De Geyer, L. Guetaz, O. Diat and G. Gebel, *Macromolecules*, 2007, **40**, 8259–8264.

14 L. Tchicaya-Bouckary, D. J. Jones and J. Rozière, *Fuel Cells*, 2002, **2**, 40–45.

15 N. Juangvanich and K. A. Mauritz, *J. Appl. Polym. Sci.*, 1998, **67**, 1799–1810.

16 Q. Deng, R. B. Moore and K. A. Mauritz, *J. Appl. Polym. Sci.*, 1998, **68**, 747–763.

17 K. A. Mauritz, *Mater. Sci. Eng., C: Biomimetic Supramol. Syst.*, 1998, **6**, 121–133.

18 M. A. Dresch, B. R. Matos, F. C. Fonseca, E. I. Santiago, M. Carmo, A. J. C. Lanfredi and S. Balog, *J. Power Sources*, 2015, **274**, 560–567.

19 E. M. Davis, J. Kim, V. P. Oleshko, K. A. Page and C. L. Soles, *Adv. Funct. Mater.*, 2015, **25**, 4064–4075.

20 M. Zatoń, J. Rozière and D. J. Jones, *J. Mater. Chem. A*, 2017, **5**, 5390–5401.

21 M. Maréchal, F. Niepceron, G. Gebel, H. Mendil-Jakani and H. Galiano, *Nanoscale*, 2015, **7**, 3077–3087.

22 K. A. Mauritz and M. K. Hassan, *Polym. Rev.*, 2007, **47**, 543–565.

23 C. Perrot, L. Gonon, C. Marestin, A. Morin and G. Gebel, *J. Power Sources*, 2010, 493–502.

24 M. Lavorgna, L. Mascia, G. Mensitieri, M. Gilbert, G. Scherillo and B. Palomba, *J. Membr. Sci.*, 2007, **294**, 159–168.

25 M. Lavorgna, M. Gilbert, L. Mascia, G. Mensitieri, G. Scherillo and G. Ercolano, *J. Membr. Sci.*, 2009, **330**, 214–226.

26 C.-Y. Yen, C.-H. Lee, Y.-F. Lin, H.-L. Lin, Y.-H. Hsiao, S.-H. Liao, C.-Y. Chuang and C.-C. M. Ma, *J. Power Sources*, 2007, **173**, 36–44.

27 H. Lin, C. Zhao, Y. Jiang, W. Ma and H. Na, *J. Power Sources*, 2011, **196**, 1744–1749.

28 N. Huynh, J. P. C. Fernandes, P. A. Bayle, M. Bardet, E. Espuche, J. Dillet, J. C. Perrin, A. El Kaddouri, O. Lottin, V. H. Mareau, H. Mendil-Jakani and L. Gonon, *J. Power Sources*, 2020, **462**, 228164.

29 H. Mendil-Jakani, I. Zamanillo Lopez, P. M. Legrand, V. H. Mareau and L. Gonon, *Phys. Chem. Chem. Phys.*, 2014, **16**, 11243–11250.

30 H. Mendil-Jakani, I. Zamanillo López, V. H. Mareau and L. Gonon, *Phys. Chem. Chem. Phys.*, 2017, **19**, 16013–16022.

31 K. Cooper, *ECS Meet. Abstr.*, 2011, DOI: 10.1149/ma2011-02/16/1043.

32 J. P. C. Fernandes, V. H. Mareau and L. Gonon, *Int. J. Polym. Anal. Charact.*, 2017, 1–7.

33 G. Orcel, L. L. Hench, I. Artaki, J. Jonas and T. W. Zerda, *J. Non-Cryst. Solids*, 1988, **105**, 223–231.

34 O. Glatter and O. Kratky, *Small-Angle X-Ray Scattering*, Academic Press Inc. Ltd, London, 1982.

35 L. A. Feigin and D. I. Svergun, *Structure Analysis by Small-Angle X-Ray and Neutron Scattering*, New York and London, Plenum Press, 1987.

36 G. Gebel, *Macromolecules*, 2013, **46**, 6057–6066.

37 A. Kusoglu and A. Z. Weber, *Chem. Rev.*, 2017, 987–1104.

38 H. Mendil-Jakani, S. Pouget, G. Gebel and P. N. Pintauro, *Polymer*, 2015, 99–107.

39 L. Rubatat, A. L. Rollet, G. Gebel and O. Diat, *Macromolecules*, 2002, 4050–4055.

40 L. Rubatat, G. Gebel and O. Diat, *Macromolecules*, 2004, 7772–7783.

41 L. Rubata and O. Diat, *Macromolecules*, 2007, **40**, 9455–9462.

42 J. C. Perrin, S. Lyonnard and F. Volino, *J. Phys. Chem. C*, 2007, 3393–3404.

43 J. C. Perrin, S. Lyonnard, F. Volino and A. Guillermo, *Eur. Phys. J.: Spec. Top.*, 2007, 57–60.

44 Y. Li, D. G. Peiffer and B. Chu, *Macromolecules*, 1993, 4006–4012.

45 K. D. Kreuer and G. Portale, *Adv. Funct. Mater.*, 2013, **23**, 5390–5397.

46 F. M. Collette, F. Thominette, H. Mendil-Jakani and G. Gebel, *J. Membr. Sci.*, 2013, 242–252.